

## RESEARCH ARTICLE

10.1002/2013JB010701

## Key Points:

- Stress-strain grain size evolution in numerical model
- Strain-hardening, strains-softening, steady state
- Calibration with rock deformation experiments

## Correspondence to:

M. Herwegh,  
herwegh@geo.unibe.ch

## Citation:

Herwegh, M., T. Poulet, A. Karrech, and K. Regenauer-Lieb (2014), From transient to steady state deformation and grain size: A thermodynamic approach using elasto-visco-plastic numerical modeling, *J. Geophys. Res. Solid Earth*, 119, 900–918, doi:10.1002/2013JB010701.

Received 23 SEP 2013

Accepted 9 JAN 2014

Accepted article online 14 JAN 2014

Published online 11 FEB 2014

## From transient to steady state deformation and grain size: A thermodynamic approach using elasto-visco-plastic numerical modeling

M. Herwegh<sup>1</sup>, T. Poulet<sup>2</sup>, A. Karrech<sup>3</sup>, and K. Regenauer-Lieb<sup>2,3</sup>
<sup>1</sup>Institute of Geological Sciences, University of Bern, Bern, Switzerland, <sup>2</sup>Australian Resources Research Center, Kensington, Western Australia, Australia, <sup>3</sup>School of Civil and Resource Engineering, University of Western Australia, Perth, Western Australia, Australia

**Abstract** Numerical simulation experiments give insight into the evolving energy partitioning during high-strain torsion experiments of calcite. Our numerical experiments are designed to derive a generic macroscopic grain size sensitive flow law capable of describing the full evolution from the transient regime to steady state. The transient regime is crucial for understanding the importance of microstructural processes that may lead to strain localization phenomena in deforming materials. This is particularly important in geological and geodynamic applications where the phenomenon of strain localization happens outside the time frame that can be observed under controlled laboratory conditions. Our method is based on an extension of the paleowattmeter approach to the transient regime. We add an empirical hardening law using the Ramberg-Osgood approximation and assess the experiments by an evolution test function of stored over dissipated energy (lambda factor). Parameter studies of, strain hardening, dislocation creep parameter, strain rates, temperature, and lambda factor as well as mesh sensitivity are presented to explore the sensitivity of the newly derived transient/steady state flow law. Our analysis can be seen as one of the first steps in a hybrid computational-laboratory-field modeling workflow. The analysis could be improved through independent verifications by thermographic analysis in physical laboratory experiments to independently assess lambda factor evolution under laboratory conditions.

## 1. Introduction

In nature, deformation under nonisostatic stress conditions and elevated temperatures often is heterogeneously distributed resulting in ductile high-strain domains, so-called shear zones [Ramsay, 1980], along which considerable displacements are accommodated. Strain is concentrated in these shear zones because elasto-visco-plastic deformation in the fault rocks (mylonites) keeps the stress low, promoting energetically optimized deformation within small rock volumes [Regenauer-Lieb and Yuen, 2003]. In order to predict the rheology of such natural shear zones, extrapolations of experiment-based flow laws toward natural conditions have to be combined with microstructural evidence of the naturally deformed tectonites.

Studies on natural and experimentally deformed monomineralic mylonites demonstrate that at given physical conditions at elevated temperatures, steady state microfabrics evolve in mylonites, where grain size, grain shape, and crystallographic orientations evolve to strain-invariant states [Barnhoorn et al., 2004; Herwegh and Handy, 1996; Means, 1981; Pieri et al., 2001]. Starting with large initial grain sizes, strength first increases to a yield value, after which strain weakening is manifest by a grain size decrease and an increase in strength of the crystallographic preferred orientation (CPO) (Figure 1; see also Pieri et al. [2001]). On the contrary, small starting grain sizes show grain growth during transient stages associated with strain hardening [Austin and Evans, 2009]. Independent of the starting grain size, a balance between grain growth and grain size reduction processes yields a characteristic grain size at high strains, i.e., at mechanical and microstructural steady state, which reflects the ambient state of stress, strain rate, and temperature [Austin and Evans, 2007; de Bresser et al., 1998, 2001; Herwegh et al., 1997]. Steady state grain sizes are closely linked to the deformation mechanisms activated in the aggregates. Small grain sizes with high surface areas promote diffusion creep, while large grains allow for grain internal plastic deformation by dislocation creep. Flow laws for these two end-member processes were explored over the last decades and are meanwhile available for a variety of different minerals [e.g., Brüggmann and Dresen, 2008; Kohlstedt et al., 1995].

Such flow laws are used for the extrapolation toward natural conditions to predict stress of rocks during deformation. As pointed out above, however, the flow laws are only calibrated for steady state deformation and not for

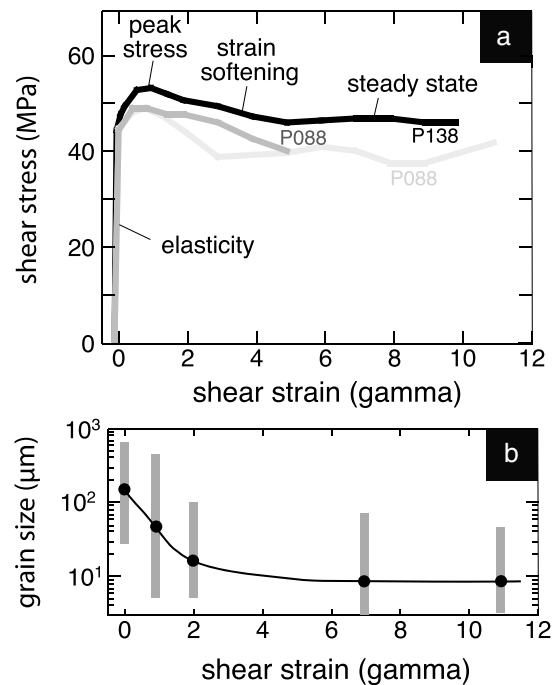


**Figure 1.** Experimental data of calcite torsion experiments from *Pieri et al.* [2001]. (a) Stress-strain curves from three experiments performed at strain rates of  $3 \times 10^{-4} \text{ s}^{-1}$  and a deformation temperature of 1000 K. (b) Corresponding grain size evolution with increasing shear strain (grey bar: grain size distribution; black dot: number-weighted mean grain sizes).

transient stages. Although few experimental studies were performed to empirically predict strain weakening of rocks during transient deformation [*Barnhoorn et al.*, 2004; *Rutter*, 1999], to our knowledge no full description exists so far in the Earth science literature to unravel the entire evolution between elastic deformation, transient elasto-visco-plastic deformation, and steady state. Knowledge on the mechanical behavior of transient deformation is rather crucial for the prediction of the onset of strain localization or renewed creep after a seismic event during the seismic cycle but also for low to intermediate strain phenomena like boudinage or folding. This gap can be closed with numerical modeling requiring reliable microphysical models that explain changes in stress and microstructure with strain. Several approaches were made to incorporate the grain size variations and their mechanical response into viscous models [*Braun et al.*, 1999; *Montési and Zuber*, 2002]. Recently, *Austin and Evans* [2007, 2009] presented the paleowattmeter, an approach which links the energy dissipated during establishing of a steady state grain size to the interplay between grain size reduction and grain growth. *Ricard and Bercovici* [2009] and *Rozel et al.* [2011] followed a similar energy-based approach by incorporating continuum mechanics and damage. All aforementioned studies are based on viscous and/or plastic deformation only. However, it is the initial elastic loading at elevated temperature that provides an important additional driving force for deformation during transient stages and the onset of dynamic recrystallization. Furthermore, the release of heat dissipated by the mechanical work of plastic deformation has a feedback on the bulk rheology and therefore also needs to be incorporated into numerical models [*Ogawa*, 1987; *Regenauer-Lieb and Yuen*, 1998, 2004; *Kaus and Podladchikov*, 2006; *Schmalholz et al.*, 2009].

*Hackl and Renner* [2013] recently published a variational analysis based on microphysics and a similar thermodynamic approach as followed here, but their study relies on the small scale (grain scale and smaller, i.e., micron to submicron-scale). The authors investigated the relation of dissipation and the steady state grain size considering various micromechanisms such as the thermodynamics of dislocations, grain size, diffusion, and elastic processes. Although such an analysis could potentially be used as input for our study, in the following we rely on relationships derived from centimeter-scale laboratory creep experiments. In doing so, we hope to indirectly capture some of the micromechanisms that are not considered in a small-scale homogenization approach. In the future we hope to merge the two approaches.

The main purpose of this paper is hence to scale up the grain-scale mechanisms to the sample size of a high-strain torsion laboratory experiment. A secondary aim is to numerically explore the transient regime because of its important control on the formation of shear zones. In order to achieve this goal, we designed and performed virtual laboratory-scale experiments. These simulations can be numerically extrapolated to geological field conditions in the future. Our work thus focuses on reproducing real laboratory experiments using a self-consistent numerical formulation.

The main purpose of this paper is hence to scale up the grain-scale mechanisms to the sample size of a high-strain torsion laboratory experiment. A secondary aim is to numerically explore the transient regime because of its important control on the formation of shear zones. In order to achieve this goal, we designed and performed virtual laboratory-scale experiments. These simulations can be numerically extrapolated to geological field conditions in the future. Our work thus focuses on reproducing real laboratory experiments using a self-consistent numerical formulation.

We did not follow the usual approach of homogenizing a discrete formulation of the problem at the microscale [e.g., *Knoll et al.*, 2009; *Cordier et al.*, 2012]. Instead, we used a formulation that is already based on the homogeneous assumption of a thermodynamic averaging of a population of grains. The average grain

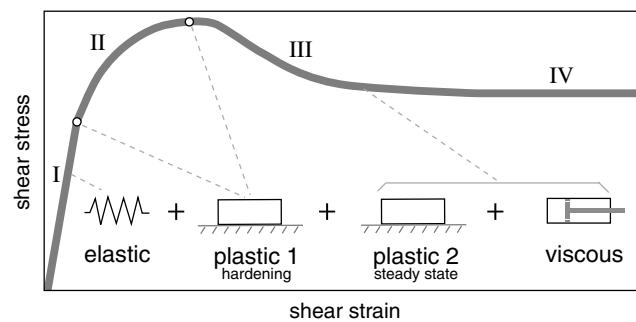


**Figure 2.** Schematic drawing illustrating thermomechanical serial coupling of the different deformation behaviors (symbols) and the region of their dominance along the stress-strain curve. The curve is characterized by initial elastic behavior (I) followed by strain hardening (II) and softening (III) and finally terminates in steady state (IV).

the method into a numerical formulation, we can explore the transient regime and the macroscale steady state evolution of rheology and grain size. This paper presents the thermodynamic approach and focuses on the discussion of the results. A concise description of the numerical aspects may be found elsewhere [Regenauer-Lieb and Yuen, 2004; Karrech et al., 2011a]. These papers deal with criteria for mesh resolution, the implementation strategy of thermodynamic approach, numerical formulation of the flow theory of plasticity, and the numerical solution technique for the elasto-visco-plastic numerical finite solver.

After an introduction into theory, the manuscript presents the setup of the shear box. Based on a parameter study and a comparison of our numerical simulations with data from high-strain high-temperature torsion experiments performed on calcite by Pieri et al. [2001], we then discuss the application of our approach to derive steady state flow laws for future applications suitable for extrapolation toward natural deformation conditions. The second step of application to a field case will be subject to a forthcoming contribution.

## 2. Theoretical Background

With the onset of deformation, differential stress will build up elastically, in a first step, followed by visco-plastic deformation. Elasticity refers to the reversible deformation of materials under stress. In the case of isotropic linear materials, this material behavior is commonly expressed by two independent material properties such as Young's modulus and Poisson's ratio ( $E$ ,  $\nu$ ), bulk and shear moduli ( $K$ ,  $\mu$ ), or the Lamé parameters ( $\lambda$ ,  $\mu$ ). Elasticity accommodates a rather limited amount of deformation, which disappears as soon as the material is unloaded. For that reason natural tectonites, exposed to the surface, do not reveal evidence for this elastic component of bulk rheology. Nonetheless, elasticity plays a fundamental role during initial loading when the stress rises (Figures 1 and 2).

After the initial elastic deformation step follows a period of a nonlinear stress increase with strain, which is called strain hardening (Figure 2). Here a variety of different deformation processes can take place as there are intracrystalline deformation by glide along active glide systems (e.g., glide-induced vorticity; see Lister and Williams [1983, and references therein]), twinning [Rutter 1974; Schmid et al., 1987], the onset of dynamic recrystallization, or even brittle processes. So far, no comprehensive microphysical models are available for the strain-hardening stage in the case of calcite.

It is important to note that we can therefore not derive the hardening behavior from thermodynamic derivations as the appropriate experiments are missing. Other materials with much simpler micromechanical behavior, such as metals, lend themselves to a much more elegant and theoretically founded analysis based on thermodynamic principles.

Because of this lack, we use an empirical homogenization of the microphysical processes by applying the Ramberg-Osgood relation [Ramberg and Osgood, 1943]. It was designed to describe the nonlinear stress-strain behavior near the peak stress (Figure 2). We follow the approach presented in Regenauer-Lieb and Yuen [2008] for the formulation of the constitutive equations and consider for all rheologies the classical isotropic elastic deformation in a corrotational Lagrangian framework (first term in equation (3) in Regenauer-Lieb and

size describes the most probable grain size at the local scale of one element, assumed to be at its state of maximum dissipation.

We developed a numerical simple shear box simulation scheme allowing the study of rheological changes for given physical deformation conditions. The shear box uses thermodynamic processes during deformation and grain homogenization based on the paleowattmeter theory [Austin and Evans, 2007, 2009]. By casting

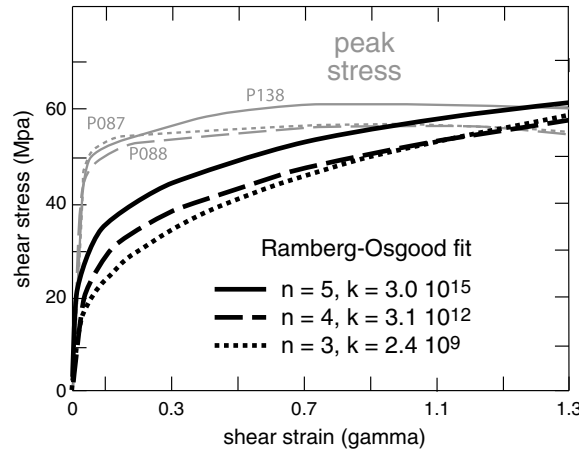


**Figure 3.** Fit of experimental data of *Pieri et al.* [2001] (grey) with the Ramberg-Osgood relation (black) to express strain hardening using equation (1) and a Young's modulus  $E$  of 72 GPa. Fit constants  $n$  and  $K$  are given at the graph's bottom.

materials science (e.g., for metals see *Skelton et al.* [1997] and *Fan et al.* [2005]) and numerical models [e.g., *Kim et al.*, 2004]. In the elastic regime, our model undergoes no permanent deformation and the stresses are below a yielding threshold. Hence,  $K$  is 0 until the norm of the stress tensor reaches the limit of elasticity. Beyond this limit hardening and visco-plasticity start playing an important role. When reaching maximum stress, strain hardening is terminated but elastic loading still continues. More details on the basic integration procedure of the elasto-visco-plastic behavior used in this paper are given in *Karrech et al.* [2011a, 2011b].

Together with strain hardening, the contribution of viscous creep and plastic deformation increases (Figure 2). During linear viscous deformation, as for example diffusion creep/granular flow, the equivalent strain rate ( $\dot{\epsilon}_{\text{diff}}$ ) linearly depends on the equivalent stress ( $\sigma$ ) (square root of the second invariant) expressed by a stress exponent of 1 (equation (2)).

$$\dot{\epsilon}_{\text{diff}} = K_{\text{diff}} \sigma^n \exp \left[ \frac{-Q_{\text{diff}}}{RT} \right] \quad (2)$$

Besides an Arrhenius-type activation term consisting of the activation energy ( $Q_{\text{diff}}$ ), the gas constant ( $R$ ), and temperature ( $T$ ), a preexponential factor ( $K_{\text{diff}}$ ) is required. Diffusion creep is particularly efficient for solid-state materials with high grain boundary area, i.e., in aggregates with small grain sizes ( $d$ ) as expressed by the negative grain size exponent  $m$ . *Austin and Evans* [2007, 2009] posit that all deformation energy is dissipated into heat having therefore no manifestation in the diffusion creep microstructure. This is not fully true, since the local production of heat will directly affect the grain growth component on the way toward a steady state microstructure. Knowledge on the energy dissipation of the individual deformation mechanisms is required and could be tracked down by approaches as published in *Karrech et al.* [2011a, 2011b, 2011c]. Microstructures related to the presence of diffusion creep are typically very fine grained and consist of equi-axed grains with no or only weak crystallographic preferred orientation [*Rutter*, 1995; *Schmid and Handy*, 1991].

For plastic deformation, i.e., dislocation creep and dislocation glide, strain rate and stress are nonlinearly related to each other (Figure 2). Among other descriptions for crystal plastic deformation (e.g., exponential creep law [*Rutter*, 1974], Peierls creep law [e.g., *Renner and Evans*, 2002]), classical power laws can be used to describe dislocation creep having the following form (equation (3)).

$$\dot{\epsilon}_{\text{dis}} = K_{\text{dis}} \sigma^n \exp \left[ \frac{-Q_{\text{dis}}}{RT} \right] \quad (3)$$

In addition to the variables mentioned above,  $K_{\text{dis}}$  is again a preexponential constant,  $n$  is the stress exponent (typically  $n > 3$ ) and  $Q_{\text{dis}}$  the activation energy for dislocation creep [e.g., *Kohlstedt et al.*, 1995; *Brügmann and Dresen*, 2008]. The intracrystalline deformation incorporates the temperature-dependent activation of glide

*Yuen* [2008]). In addition we expand the approach here to include a hardening term of plastic strain of the Ramberg-Osgood formulation.

$$\epsilon^{\text{RG}} = K \left( \frac{\sigma_y}{E} \right)^m \quad (1)$$

where  $\epsilon^{\text{RG}}$  is the equivalent strain (square root of the tensor's second invariant) during Ramberg-Osgood hardening,  $\sigma_y$  is the second invariant of the deviatoric stress tensor, and  $E$  represents Young's modulus.  $K$  and  $m$  are dimensionless constants, which describe the hardening behavior in the plastic regime. Typical values for  $m$  are between 3 and 5 (Figure 3). Note that the Ramberg-Osgood equation is widely applied in

systems in the crystals. With strain, a buildup of defect structures like screw dislocations is manifest as a result of the mechanical work. Since this work controls microstructural parameters like the recrystallized grain size and either requires or delivers energy, the link between mechanical action and required energy budget needs to be established. The specific internal energy of these intracrystalline processes is given in terms of the specific entropy  $s$  by

$$u = \psi(T, \varepsilon_{ij}^{\text{el}}, d) + sT \quad (4)$$

here  $u$  is the specific internal energy of the system,  $\psi$  the specific Helmholtz free energy as a function of  $T$  the temperature,  $\varepsilon_{ij}^{\text{el}}$  the elastic strain, and  $d$  the grain size. In terms of an energy budget, time-dependent evolution of  $\psi$  has to be derived (equation (5)).

$$\dot{\psi}(T, \varepsilon_{ij}^{\text{el}}, d) = \left( \frac{\partial \psi}{\partial T} \right)_{\varepsilon_{ij}^{\text{el}}, d} \dot{T} + \left( \frac{\partial \psi}{\partial \varepsilon_{ij}^{\text{el}}} \right)_{T, d} \dot{\varepsilon}_{ij}^{\text{el}} + \left( \frac{\partial \psi}{\partial d} \right)_{\varepsilon_{ij}^{\text{el}}, T} \dot{d} \quad (5)$$

In the above equation the subscripts  $i$  and  $j$ , which take the values 1, 2, and 3, denote the directions of the Euclidian space. Note that we use the convention of summation indices in this paper.

Related to the mechanical work performed during plastic deformation, heat is liberated. This additional heat reduces the strength of the temperature-dependent rheology of the deforming material and simultaneously increases the grain growth rate. Hence, the establishment of the balance between grain growth and grain size reduction during steady state creep correlates directly with the energies provided by the mechanical work. Such a link is called a thermomechanical feedback. The total dissipative work appearing as a first feedback in form of shear heating can be calculated as a function of time (equation (6))

$$\chi_{(t)} \sigma_{ij} \dot{\varepsilon}_{ij}^{\text{diss}} = \sigma_{ij} \dot{\varepsilon}_{ij} - \rho \frac{\partial \psi}{\partial \varepsilon_{ij}^{\text{el}}} \dot{\varepsilon}_{ij}^{\text{el}} - \rho \frac{\partial \psi}{\partial d} \dot{d} \quad (6a)$$

where  $\chi_{(t)}$  is the Taylor-Quinney coefficient,  $\dot{\varepsilon}_{ij}^{\text{diss}}$  is the dissipative strain rate, and  $\rho$  is density. In the particular case when  $\sigma_{ij}$  is the thermodynamic force conjugate of the deformation both in the permanent and reversible regimes, the above equation, reduces to the following:

$$\chi_{(t)} \sigma_{ij} \dot{\varepsilon}_{ij}^{\text{diss}} = \sigma_{ij} \dot{\varepsilon}_{ij}^{\text{p}} - \rho \frac{\partial \psi}{\partial d} \dot{d} \quad (6b)$$

where  $\dot{\varepsilon}_{ij}^{\text{p}}$  is the rate of permanent deformation. The second term is the stored energy of grain size reduction, which is consequently not available for shear heating; hence, it belongs to the stored energy of cold work [Rosakis et al., 2000]. In the same way, Hooke's law of elasticity can be obtained as the derivative of Helmholtz free energy with respect to the elastic deformation:  $\sigma_{ij} = \rho \frac{\partial \psi}{\partial \varepsilon_{ij}^{\text{el}}}$ . We emphasize that an often overlooked second feedback term  $\phi$  follows from the thermodynamic approach which considers the grain size evolution with time and links the stored (Helmholtz free) energy to the partial derivatives of grain size and temperature (Figure 4).

$$\phi = \rho T \frac{\partial^2 \psi}{\partial d \partial T} \dot{d} \quad (7)$$

As mentioned earlier, Hooke's law of elasticity is used in the elastic regime. This regime is delimited by an envelope written in terms of the norm of the stress tensor as follows:  $f(\sigma_{ij}) = \sigma_{\text{eq}} - \sigma_0$ , where  $\sigma_0$  is threshold beyond which the material starts yielding and dissipative deformations start taking place. For simplicity, we considered the Von Mises criterion as it is valid for geomaterials undergoing deformations at high temperatures. The threshold  $\sigma_0$  depends on the permanent deformation in accordance with the Ramberg-Osgood formula. On the other hand, the equivalent stress  $\sigma_{\text{eq}}$  is calculated by inversion knowing the rate of deformation, temperatures, and the expressions of the viscous flow laws, which are presented in the following section.

### 3. Implementation of Grain Size Evolution

Austin and Evans [2007, 2009] postulate that the plastic energy stored in the microstructure is manifest by the grain size. These authors assume that the grain sizes evolve over time scales less than those for stress variations and that the rate of increase of internal energy is related to the rate of increase in grain boundary

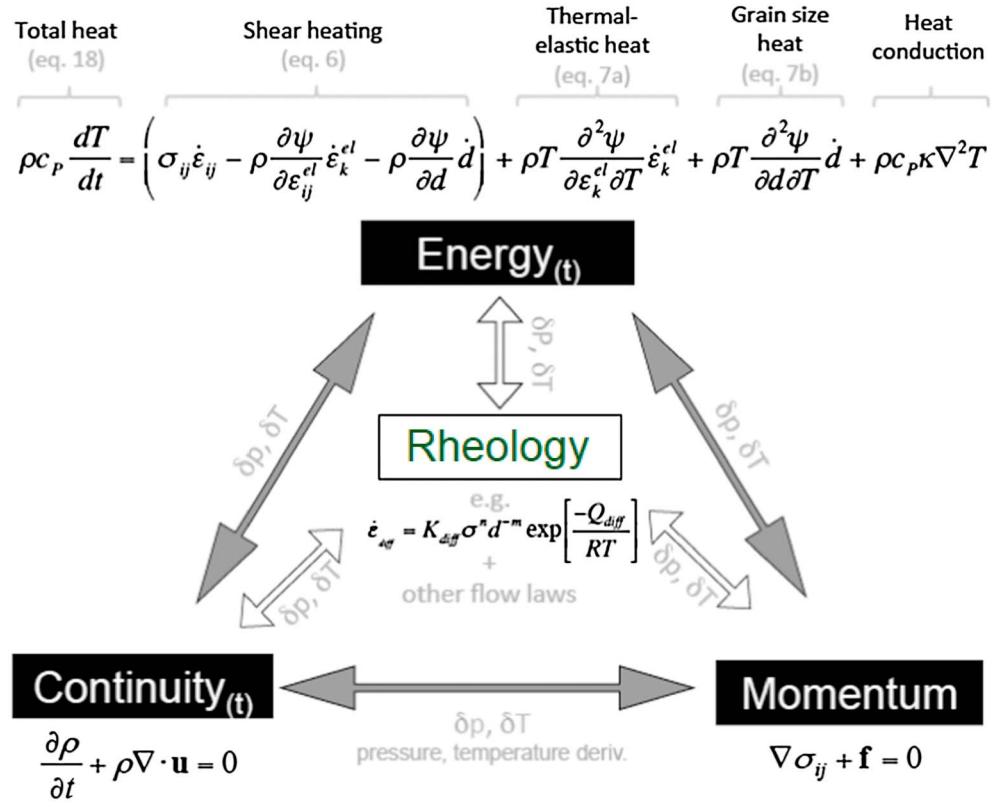


**Figure 4.** Schematic overview shows the two principal types of feedbacks, their interactions, and the equations. (i) Fundamental feedbacks (grey arrows) between energy, continuity, and momentum. (ii) Material feedbacks (white arrows) related to the bulk rheology, which consists of four mechanical components placed in series: elasticity, Ramberg-Osgood strain hardening, dislocation creep, and diffusion creep (see text for explanations).

area [see *Austin and Evans, 2009*, equation 19]. Transferring to our aforementioned notation of the Helmholtz free energy yields

$$\dot{\psi}(T, \epsilon_{ij}^{el}, d) = -\frac{c\gamma}{d^2} \dot{d}_{red} \quad (8)$$

where  $\gamma$  is the average specific grain boundary energy,  $c$  is a geometric constant, and  $\dot{d}_{red}$  is the rate of change of the grain boundary area during grain size reduction via dynamic recrystallization. It follows from taking the time derivative of equation (4) that

$$\dot{u} = \dot{\psi}(T, \epsilon_{ij}^{el}, d) + \dot{s}T + \dot{T}s \quad (9)$$

assuming isothermal conditions, it follows that

$$\dot{T}s = 0 \quad (10)$$

$$\dot{s}T = (1 - \beta)\sigma_{ij}\dot{\epsilon}_{ij} + (1 - \lambda_{dis})(\beta)\sigma_{ij}\dot{\epsilon}_{ij} \quad (11)$$

$$\text{where } \beta = \frac{\dot{W}_{dis}}{\dot{W}_{tot}} \quad (12)$$

is the ratio of the dissipated power of dislocation creep over the total power dissipation ( $\dot{W}_{tot} = \sigma \dot{\epsilon}_{tot} = \sigma \dot{\epsilon}_{dif} + \sigma \dot{\epsilon}_{dis}$  and  $\dot{W}_{dis} = \sigma \dot{\epsilon}_{dis}$ ). The parameter  $\lambda_{dis}$  represents the portion of power input by dislocation creep strain rate, which increases the internal energy [see *Austin and Evans [2009]*]. Note that in comparison to the thermodynamic notation (equation (6))  $1 - \lambda_{dis}$  represents the Taylor-Quinney coefficient  $\chi_{(t)}$ . The  $\dot{s}T$  of equation (11) reflects the rate of dissipation during a relative partitioning of strain rate between diffusion creep and dislocation creep and the efficiency of the two processes [Austin and Evans, 2009, equation 21]. While the power input



during diffusion creep is assumed to be completely dissipated ( $\lambda_{\text{diff}} = 0$ , see argumentation in *Austin and Evans* [2009]), a portion of the power input during dislocation creep is stored in the microstructure ( $0 < \lambda_{\text{dis}} < 1$ ).

In terms of grain size evolution, *Austin and Evans* [2009] expressed the rate change in total grain size  $\dot{d}_{\text{tot}}$  as the sum of contribution of the rates in grain size reduction  $\dot{d}_{\text{red}}$  and grain growth  $\dot{d}_{\text{growth}}$  (equation (13)).

$$\dot{d}_{\text{tot}} = \dot{d}_{\text{red}} + \dot{d}_{\text{growth}} \quad (13)$$

The rate  $\dot{d}_{\text{red}}$  is expressed as

$$\dot{d}_{\text{red}} = \frac{-\beta \lambda \sigma \dot{\epsilon} d^2}{c\gamma} \quad (14)$$

where  $\lambda$  is the energy fraction deposited in the microstructure. The rate  $\dot{d}_{\text{growth}}$  can be expressed by a classical Arrhenius-type growth law

$$\dot{d}_{\text{growth}} = K_g \exp\left(\frac{-Q_g}{RT}\right) p^{-1} d^{1-p} \quad (15)$$

$K_g$  is the preexponential factor,  $Q_g$  the activation energy, and  $p$  the grain size exponent of the grain growth law. Substituting (i) equations (14) and (15) in equation (13), (ii) using the dislocation creep law (equation (3)), and (iii) assuming  $\dot{d}_{\text{tot}}$  equals to zero at steady state results in the final paleowattmeter equation for the steady state grain size of [Austin and Evans, 2007, 2009]

$$d_s = \kappa \cdot \sigma^{-m'} \cdot \exp\left(-\frac{Q}{RT}\right) \quad (16)$$

where

$$\kappa = \left[\frac{c\gamma K_g}{\lambda p K_{\text{dis}}}\right]^{\frac{1}{p+1}}, m' = \left[\frac{n+1}{p+1}\right], \text{ and } Q = \frac{Q_g - Q_{\text{dis}}}{(p+1)}$$

In this sense, we can base our numerical model on the energy dissipation of the different deformation terms (equations (2)–(5)), their feedback mechanisms shown in Figure 4 (equations (6) and (7)), the rates of grain size reduction (equation (14)), and grain growth (equation (15)) on the way toward a strain-invariant steady state grain size (equation (16)).

In summary, this leads to the following bulk rheology

$$\dot{\epsilon}_{ij}^{\text{total}} = \dot{\epsilon}_{ij}^{\text{el}} + \dot{\epsilon}_{ij}^{\text{RG}} + \dot{\epsilon}_{ij}^{\text{diff}} + \dot{\epsilon}_{ij}^{\text{dis}} \quad (17)$$

with the total energy equation

$$\rho c_p \frac{dT}{dt} = \left( \sigma_{ij} \dot{\epsilon}_{ij} - \rho \frac{\partial \psi}{\partial \epsilon_{ij}^{\text{el}}} \dot{\epsilon}_{ij}^{\text{el}} - \rho \frac{\partial \psi}{\partial d} \dot{d} \right) + \rho T \frac{\partial^2 \psi}{\partial \epsilon_{ij}^{\text{el}} \partial T} \dot{\epsilon}_{ij}^{\text{el}} + \rho T \frac{\partial^2 \psi}{\partial d \partial T} \dot{d} + \kappa \nabla^2 T \quad (18)$$

where  $\kappa$  is the thermal diffusivity of the last term (the conduction term) in the energy equation. Note that we use a Lagrangian formulation where the material derivatives and therefore heat advection is implicitly considered. We do not consider any other additional heat sources such as radioactive/Joule/chemical reaction heating. As illustrated in Figure 4 this introduces two fundamental types of feedback; one is the basic feedback mechanism between the energy, continuity, and momentum equations, and the other is the additional feedback through the material state including grain size as a thermodynamic state variable. The role of feedback mechanisms is pivotal for adjusting the system to a grain size distribution achieving a new quasi-steady state which is an output of the numerical solution of the new far from equilibrium thermodynamic state. In other words this paper extends the paleowattmeter approach into a new numerical formulation for deriving constitutive behavior from laboratory experiments.

#### 4. Model Setup and Constraints

When dealing with grain size modeling, two fundamentally different approaches can be used. One approach is to deal with the individual interactions between the grains explicitly and use the theory of statistical mechanics (e.g., Elle model, see *Jessell et al.* [2001, 2009] and *Bons et al.* [2008]). The other approach is to use a continuum mechanics framework where the laws of thermodynamics apply. This means that instead of a single grain a

**Table 1.** Experimental Flow Laws and Associated Parameters for Calcite<sup>a</sup>

Type	Flow Law	Parameters
Dislocation creep [Schmid <i>et al.</i> , 1980]	$\dot{\epsilon}_{dis} = K_{dis} \cdot \sigma^{n_{dis}} \cdot \exp\left[\frac{-Q_{dis}}{RT}\right]$	$K_{dis} = 2511.9 \text{ MPa}^{-n_{dis}} \text{ s}^{-1}$ $n_{dis} = 4.7$ $Q_{dis} = 297 \text{ kJ/mol}$
Diffusion creep [Herwegh <i>et al.</i> , 2003]	$\dot{\epsilon}_{dif} = K_{dif} \cdot \sigma^{n_{dif}} \cdot d^{-m} \cdot \exp\left[\frac{-Q_{dif}}{RT}\right]$	$K_{dif} = 4.3e7 \text{ MPa}^{-n_{dif}} \mu\text{m}^{-m} \text{ s}^{-1}$ $n_{dif} = 1.1$ $m = -3.3$ $Q_{dif} = 200 \text{ kJ mol}^{-1}$

<sup>a</sup> $\dot{\epsilon}_{dis}$  and  $\dot{\epsilon}_{dif}$  are strain rate,  $K_{dis}$  and  $K_{dif}$  are the preexponential constants,  $\sigma$  is the stress,  $n_{dis}$  and  $n_{dif}$  are the stress exponents,  $d$  is the grain size,  $m$  is the grain size exponent,  $Q_{dis}$  and  $Q_{dif}$  are the activation energies,  $R$  is the gas constant, and  $T$  is the temperature in K.  $d$  is ten percent of experimental uncertainty inferred since no error estimates are given in the original study.

population distribution of grains must be modeled. The size of an individual element that contains a number of grains must be large enough that a population density function is relevant. This size is equivalent to a size where the grain size distribution can be used by a thermodynamic averaging technique. Note that this approach is exactly analogous to the thermodynamic definition of pressure where when only a few atoms are described a full molecular dynamics calculation must be done and there are collisions between individual atoms which must be considered. The homogenized term pressure, however, only has a meaning when the number of collisions between atoms is large enough for a thermodynamic description. Also, the use of a mathematical formulation based on shear stress and pressure implicitly implies a thermodynamic averaging.

It is therefore important to note that when we talk in the following about a grain size, we always refer to an individual average cell grain size. Note that this grain size is virtually averaging over an undefined number of grains within this cell. Hence, on the size of the individual cell, it is not possible to obtain information on the form of the grain size distribution function. This is not necessary for our approach since, in contrast to high-resolution microstructure-based models, we intend to resolve neither grain interactions on the scale of grain boundaries nor the size changes of single individual grains. Compared to a real microstructure, our numerical model represents a population density function of a number of individual grains. Hence, when our average cell grain size grows, within the virtual aggregate some grains grow but others would have to shrink in order to maintain compatibility. Note that although it is not possible to resolve the grain size population within a model cell, the grain size distribution function of the bulk aggregate is available by integrating over the grain size averages of all cells of the numerical model.

In the current approach the finite element modeling software ABAQUS is used, which is expanded by user-defined material models (UMAT) [Karrech *et al.*, 2011a, 2011b, 2011c]. The UMAT was adapted in this study to allow for the thermomechanical coupling between elastic, viscous, and plastic deformation in calcite. For this

**Table 2.** Laws for Grain Growth and Grain Size Reduction Terms of Calcite<sup>a</sup>

Type	Law	Parameters	Treatment in Model
Grain growth	$\dot{d}_{growth} = K_g \exp\left(\frac{-Q_g}{RT}\right) p^{-1} d^{1-p}$	$K_g = 2511.9 \text{ MPa}^{-n_{dis}} \text{ s}^{-1}$ $Q_g = 175 \text{ kJ mol}^{-1}$ $R = 8.314 \text{ J mol}^{-1}$ $T$ $d$ $p = 3$	fixed from grain growth experiment fixed from grain growth experiment fixed value input parameter calculated from previous time step fixed from grain growth experiment
Grain size reduction	$\dot{d}_{red} = \frac{-\beta \lambda \sigma \dot{\epsilon} d^2}{c \gamma}$ where $\beta = \dot{\epsilon}_{dis} / \dot{\epsilon}_{tot}$	$\beta$ $\lambda = 0.1$ or $0.001-0.1$ $\sigma$ $\dot{\epsilon}$ $d$ $c = \pi$ $\gamma = 1 \text{ J m}^{-2}$	calculated for each time step held constant or is ramped (see text) calculated for each time step calculated for each time step calculated for each time step fixed value fixed value

<sup>a</sup>Fixed parameters are taken from Covey-Crump [1997] for grain growth or from Austin and Evans [2007, 2009] for the grain size reduction term.  $\dot{d}_{growth}$  and  $\dot{d}_{red}$  are rates for grain growth and grain size reduction, respectively.  $K_g$  is a preexponential constant of the grain growth law,  $d$  is the grain size at the given time increment,  $p$  is the grain size exponent,  $Q_g$  is the activation energy for grain growth,  $R$  is the gas constant, and  $T$  is the temperature in K.  $\lambda$  is the fraction of energy dissipated in formation of the microstructure,  $\sigma$  is the stress exponent,  $\dot{\epsilon}$  is the total strain rate at the given time increment,  $c$  is a geometric constant, and  $\gamma$  is the grain boundary energy.



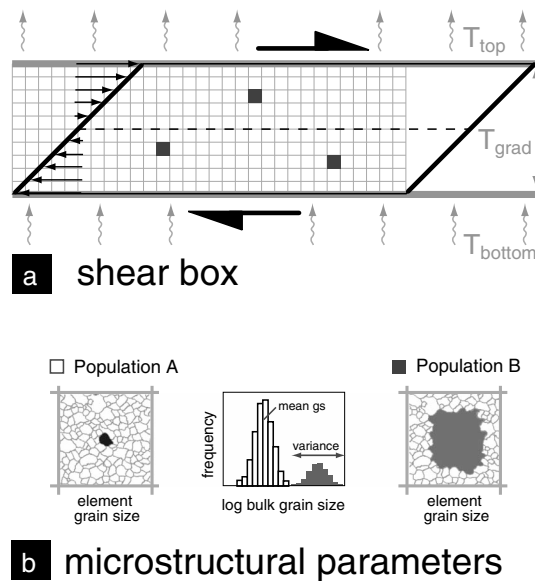


**Figure 5.** (a) Shear box geometry with ratio of width to length of 1:3, thermal top and bottom boundaries, and fixed side boundaries that displace at constant velocities. Gridlines indicate element dimensions in the case of a  $10 \times 30$  model. (b) Individual grain size values of small (grey) and large-sized (empty) grain populations are randomly distributed over the entire element set. Note that a value of a single grain size is attributed to each element, whereas the element dimensions are much larger compared to the grain size.

purpose a Young's modulus of  $7.5 \times 10^{10}$  Pa was used and experimental calibrations were incorporated using dislocation and diffusion creep flow laws of Schmid *et al.* [1980] and Herwegh *et al.* [2003], respectively (Table 1). To describe the strain-hardening part (Figure 2), the Ramberg-Osgood relation was calibrated on the basis of mechanical data from calcite torsion experiments performed by Pieri *et al.* [2001]. Best fits were obtained for  $K = 3 \times 10^{15}$  and  $m = 5$  (Figure 3). The transition from strain-hardening part to perfect plastic behavior has to be predefined at the present stage (see Figure 2 and below).

In order to link the evolution in grain size with rheology, the paleowattmeter approach of Austin and Evans [2007, 2009] was implemented. In the numerical models the grain sizes evolve by thermomechanical coupling following the grain size reduction and grain growth rates of equations (14) and (15), originally defined in Austin and Evans [2007, 2009] (for parameters, see Table 2).

In terms of model setup, a shear box is defined by the ratio of height to width of 1:3 allowing simple shear deformation (Figure 5a). The model has fixed velocity boundary conditions forcing the side boundaries of the shear box to move at predefined velocity (Figure 5a). This velocity is calculated to be in agreement with bulk strain rates required for the appropriate scale and deformation conditions to be modeled ( $\sim 10^{-3}$  to  $10^{-5} \text{ s}^{-1}$  for experiments and  $10^{-9}$  to  $10^{-14} \text{ s}^{-1}$  for nature). To simulate experimental and natural situations, various thermal boundary conditions are implemented. Depending on the scale of the application of the shear box, i.e., centimeter- versus kilometer-size dimensions, thermal boundaries of the model can be fixed to different values on model's bottom and top (Figure 5). In this way a heat flux across the shear box can be generated that is in accordance with the appropriate geothermal gradient (e.g.,  $30^\circ\text{C}/\text{km}$ ). We describe in this paper only a formulation for shear strains smaller than 1. A different continuum formulation must be used for higher strains that include logarithmic elastic rotations as implemented in Karrech *et al.* [2011c]. Therefore, the present model is not cyclic in  $X$  and  $Y$  directions.

Within the shear box the size of the individual elements can be varied. For this study, mostly an array of  $30 \times 10$  and in a few cases  $60 \times 20$  and  $120 \times 40$  elements was used. All three grids served for a grid sensitivity study (see below). Note that for all applications, the element dimensions are much larger than the final steady state grain size of the samples to be modeled (Figure 5b). Hence, the model is not designed to investigate processes on the resolution of individual grains or grain boundaries (e.g., Elle model see Jessell *et al.* [2001]) but rather picks out a statistically sufficient number of grains of an aggregate with infinite dimensions and predicts what the grain size evolution is following the aforementioned mechanical and microstructural laws. In this sense, each finite element has to be thought of as an average of local grain sizes that cannot be resolved any further.

At the present stage, two different grain size populations and their grain size distributions can be generated to define the starting material of each model consisting of small and large grain sizes (Figure 5b). The input requires definition of the volume fraction and the average and standard variation of grain size distribution of each population. The strategy to use coarse- and fine-grained populations allows monitoring of both variations of the local stress state (grain size versus grain size insensitive deformation) and the convergence of the grain sizes toward steady state. For example, starting grain sizes too small compared to the steady state will grow and deform under the corresponding deformation mechanism, which either is diffusion creep or a combination of

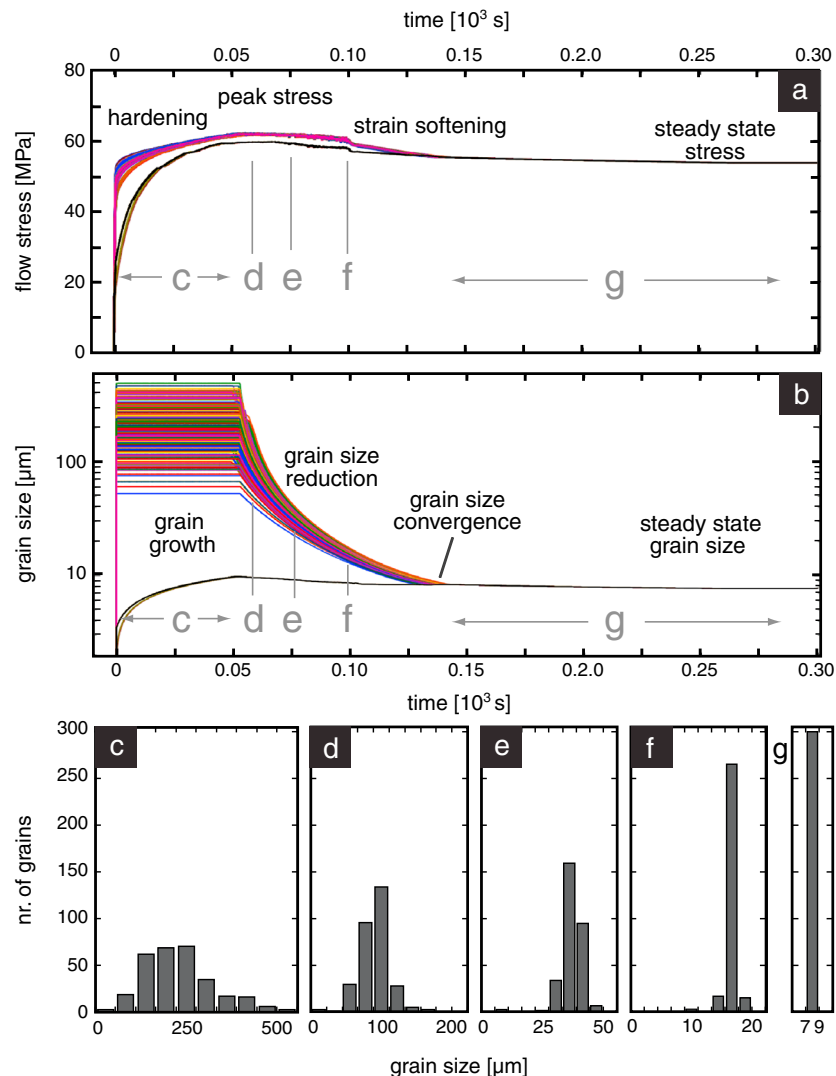


**Figure 6.** Numerical model with temperature = 1000 K, strain rate =  $1 \times 10^{-4} \text{ s}^{-1}$ , and a  $\lambda$  ramp from 0 to 0.4 over a shear strain of 0.26 (see text for explanation). (a) Stress-strain and (b) grain size-strain curves for each of the 300 grains. Note the grain growth (particularly visible for small grains) during the first  $0.05 \times 10^3 \text{ s}$  (Figure 6b), which is associated with continuous strain hardening. At peak stress, grain size reduction in the large grains starts following the paleowattmeter relationship resulting in strain weakening (compare Figures 6a and 6b). Once the shrinking large and growing small grains converge, steady state grain size and steady state stress are established. Grain size distributions (c) at the start of the experiment, (d, e, f) during grain size reduction, and (g) at steady state.

diffusion and dislocation creep, the latter being the case once the grain size is close to steady state. In contrast, grain sizes too big will shrink and deform under dislocation creep. In the current models, the volume fraction of the grain size population of rheological interest is set to 0.99 to ensure that the subordinate grain size population has no dominant effect on the bulk rheology but still allows the documentation of the grain size convergence on the way to steady state. Note that the continuous monitoring of this convergence in a single model run is one of the great advantages of the numerical approach compared to studies of experimentally or naturally deformed real rocks, where only few time steps or even just the final stage of a long-lasting evolution is preserved.

For each time increment and each individual element the mechanical state (i.e., stress, strain rate, contribution of dislocation/diffusion creep, local temperature, and grain size) is determined and stored. These parameters can be read out and used for further data processing and data analysis.

The approach has been followed to explore the general performance of the model in comparison to the high-strain torsion experiments of calcite *Pieri et al.* [2001]: (i) First, models were run on the basis of the

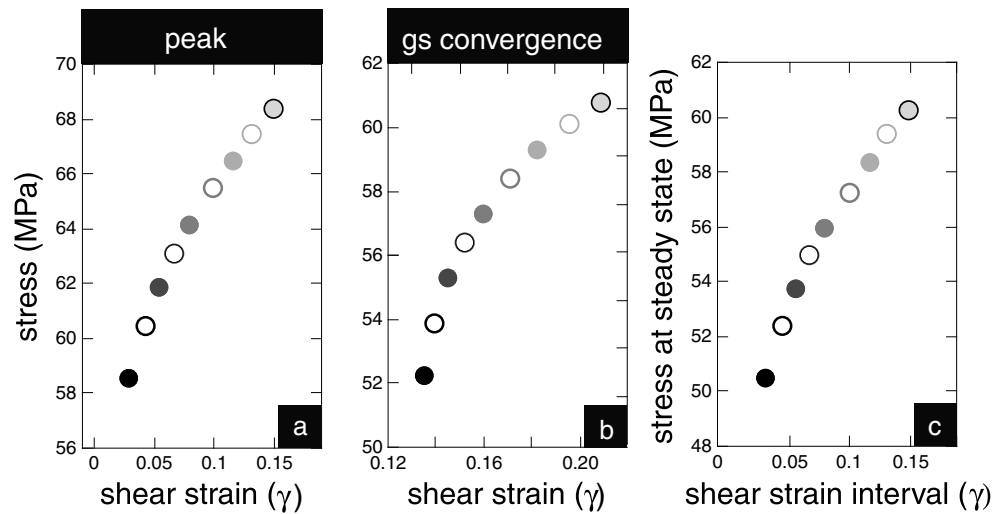


**Figure 7.** Relationship between duration of Ramberg-Osgood strain hardening and subsequent stresses (a) at peak conditions, (b) at the time of grain size convergence, and (c) at steady state stresses as a function of shear strain during which Ramberg-Osgood strain hardening was active. Note that in Figures 7a and 7b the actual stresses at the given shear strains (x axis) are displayed, while in Figure 7c the relation between shear strain at the end of Ramberg-Osgood hardening and the final steady state stress is presented. Individual symbols correspond to the same numerical experiment, facilitating the comparison among Figures 7a–7c. Bulk stress is obtained by averaging over the stress states of all individual grains.

aforementioned torsion experiments using their strain rate, temperature, and starting grain size distribution as input parameters. (ii) In order to check for the parameters responsible for peak stress, strain weakening, steady state stress, and the corresponding shape of the stress-strain curve as well as of the steady state grain size, individual parameters were varied while keeping the others constant. (iii) In a last step a grid sensitivity study was carried out to learn more about required grid spacing in light of thermomechanical predictions.

## 5. Results

### 5.1. General Model

For the first model run a temperature of 1000 K, a strain rate of  $1 \times 10^{-4} \text{ s}^{-1}$ , and a lambda of 0.4 were chosen, the latter ramping from 0 to 0.4 during a shear strain increment of 0.26 (Figure 6). In accordance with the

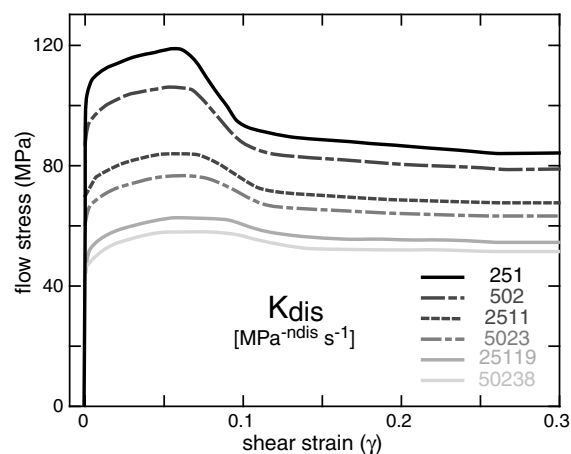


**Figure 8.** Changing stresses with increasing shear strain for numerical experiments subjected to variations in the preexponential parameter ( $K_{dis}$ ) of the dislocation creep component. Experiments were performed at  $T = 1000 \text{ K}$  and with a ramping  $\lambda$  from 0 to 0.4 during the shear strains from 0 to 0.26. Bulk stress is obtained by averaging over the stress states of all individual grains.

high-strain torsion experiments of *Pieri et al.* [2001], the model starts with 297 elements simulating large grains, showing a Gaussian grain size distribution around a mean grain size of  $200 \mu\text{m}$  (Figure 6c). In order to document the grain size evolution of both small and large grains, three elements simulating small grains with initial sizes smaller than  $10 \mu\text{m}$  were added. Figures 5b and 5a represent the changes in stress and in grain size for each individual grain, respectively. During initial elastic loading, all grains undergo grain growth while they deform by strain hardening in a Ramberg-Osgood manner and a limited contribution of viscous deformation (Figures 6a and 6b). Due to limited size changes and the logarithmic scale, however, grain growth is visible at the

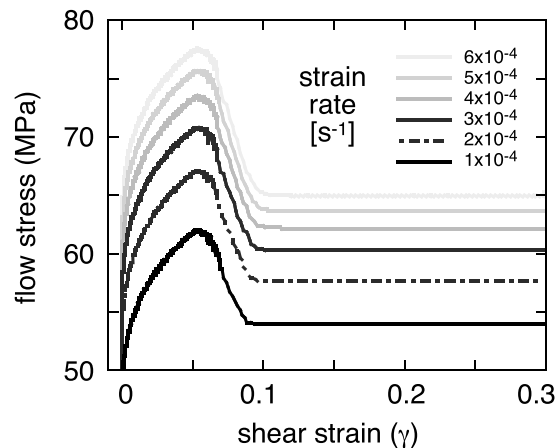


**Figure 9.** Changes in stresses with increasing strain for experiments performed at different strain rates ranging from  $1 \times 10^{-4} \text{ s}^{-1}$  to  $6 \times 10^{-4} \text{ s}^{-1}$ . For all experiments,  $T = 1000 \text{ K}$  and  $\lambda = 0.4$ . Bulk stress is obtained by averaging over the stress states of all individual grains.

deformation experiment (Figure 1) and the numerical simulation (Figure 6). Strain distribution during these transient stages is heterogeneous particularly around those cells characterized by small grain sizes. With progressive strain and grain size reduction, the heterogeneity disappears and deformation becomes homogeneous. A more detailed treatment of the strain localization behavior is beyond the scope of the present paper and will be discussed elsewhere.

Both steady state mean grain size and bulk stress are close to the experimentally obtained values (compare Figures 1 and 6). The main difference between rock deformation experiment and numerical model using standard flow laws is the lower shear strain required in the latter to reach peak and steady state stress. This discrepancy indicates either that the steady state flow laws are too weak for describing transient deformation or there are differences between the kinetics of grain size reduction processes between the rock deformation and numerical experiments. To discriminate between the two possibilities, a sensitivity study was carried out for the numerical approach to unravel the most important parameters affecting peak stress during transient stages and steady state stress in the case.

## 5.2. Parameter Study

In order to understand how the different parameters affect the grain size reduction and mechanical evolution, one key parameter per experiment was changed, while the rest of the input variables were kept constant. Given

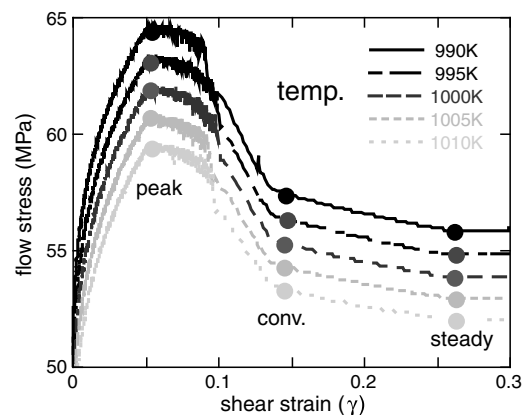


**Figure 10.** Variations in stress with increasing shear strain for deformation temperatures ranging from 990 to 1010 K. Experiments were carried out at constant strain rates of  $1 \times 10^{-4} \text{ s}^{-1}$  and with a  $\lambda$  ramp from 0 to 0.4 during the shear strains from 0 to 0.26. Bulk stress is obtained by averaging over the stress states of all individual grains.

presented scale for small grains only (Figure 6b, see lower part). With termination of Ramberg-Osgood hardening near peak stress (61.9 MPa), rate-dependent plastic deformation dominates and so the grain size reduction starts for grains being too large compared to the steady state grain size (compare Figures 6a and 6b with 6d–6f). In fact all grains, even the initially small ones, undergo grain size reduction in this experiment following the paleowattmeter relation of Austin and Evans [2007, 2009]. Grain size reduction is accompanied by strain weakening (Figure 6a). Once the grain sizes converge toward the steady state grain sizes of  $7.7 \mu\text{m}$  (Figures 6b and 6g), stresses also reach a stable value of 53.8 MPa (Figure 6a). Note the excellent agreement in grain size reduction and steady state grain size between rock

deformation experiment and numerical simulation (Figure 6). Strain distribution during these transient stages is heterogeneous particularly around those cells characterized by small grain sizes. With progressive strain and grain size reduction, the heterogeneity disappears and deformation becomes homogeneous. A more detailed treatment of the strain localization behavior is beyond the scope of the present paper and will be discussed elsewhere.

## 5.3. Strain-Hardening Component

In our setup, the Ramberg-Osgood relation defines strain hardening (equation (1), see above). Although we kept variables  $K$

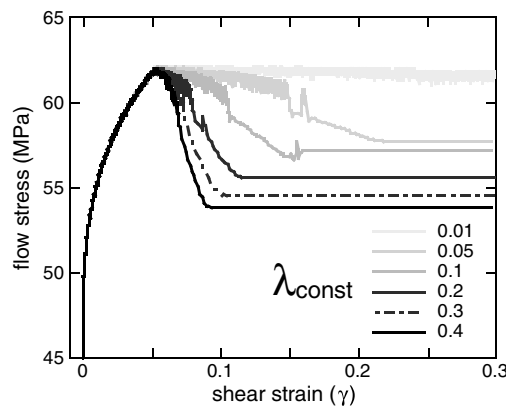


**Figure 11.** Shear strain versus stress calculated for constant  $\lambda$  of 0.01–0.4. Note that the larger the  $\lambda$ , the more pronounced the strain softening induced stress drops and the shorter the strain intervals required to achieve steady state. Strain rate of  $1 \times 10^{-4} \text{ s}^{-1}$  and  $T = 1000 \text{ K}$ . Bulk stress is obtained by averaging over the stress states of all individual grains.

experimentally determined variables in this equation. Errors of more than 1 order of magnitude must be considered when dealing with  $K_{\text{dis}}$ . Starting from the original value of  $2511 \text{ MPa}^{-\text{ndis}} \text{ s}^{-1}$  [see Austin *et al.*, 2008], we varied  $K_{\text{dis}}$  from 251 to  $50,238 \text{ MPa}^{-\text{ndis}} \text{ s}^{-1}$  (Figure 8). The lower the  $K_{\text{dis}}$ , the larger stress at peak and steady state stress (Figure 8). The minimum value of  $K_{\text{dis}} = 251$  yields 118 MPa and 83 MPa for peak and steady state, while  $K_{\text{dis}} = 50,238$  results in 57 and 51 MPa, respectively. Hence, by varying  $K_{\text{dis}}$ , both the peak values and the degree of post-peak strain weakening are controlled.

#### 5.5. Strain Rates ( $\dot{\epsilon}$ )

Strain rates from rock deformation experiments are calculated by measuring the dimensional change after an experiment to estimate bulk strain dividing this value by the duration of deformation. Also, this estimation bears uncertainties. For the numerical experiments, we varied the strain rates by increasing the strain rate by steps of  $1 \times 10^{-4} \text{ s}^{-1}$  from  $1 \times 10^{-4} \text{ s}^{-1}$  to  $6 \times 10^{-4} \text{ s}^{-1}$  (Figure 9). Generally, the slower the strain rate, the lower

and  $m$  of equation (1) constant, we varied the duration of the hardening activity ranging from shear strains of 0.03 to 0.15 (Figure 7). Increasing strain increments of strain hardening results not only in an increase in peak stress but also in the stresses at the grain size convergence and even at the final stress during steady state (Figures 7a–7c). The absolute differences in the obtained stress are about 10 MPa for the range in shear strains considered for strain-hardening activity.

#### 5.4. Preexponential Parameter of Dislocation Creep ( $K_{\text{dis}}$ )

Using a series of real rock deformation experiments, the preexponential factor ( $K_{\text{dis}}$ ) is calculated by solving equation (3). This parameter is subjected to considerable variability due to the error propagation related to each of the exper-

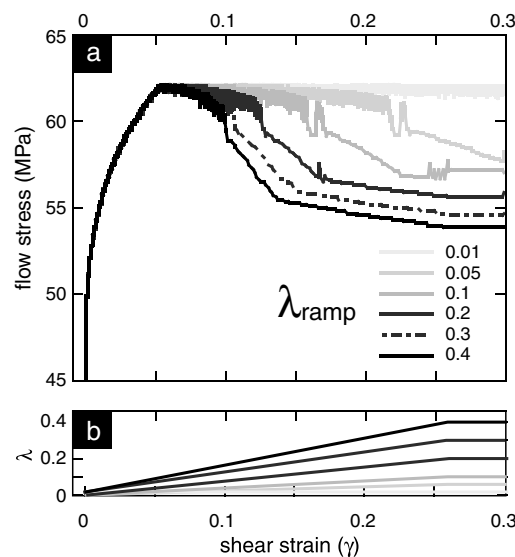


**Figure 12.** (a) Shear strain versus stress calculated for ramping  $\lambda$  from 0 to 0.01–0.4. (b) The  $\lambda$  values increase from 0 to the final value during the first 0.26 $\gamma$ . Stress drops during strain softening are identical to those found in constant  $\lambda$  experiments, but the timing of the onset of steady state expands to larger shear strains. Strain rate of  $1 \times 10^{-4} \text{ s}^{-1}$  and  $T = 1000 \text{ K}$ . Bulk stress is obtained by averaging over the stress states of all individual grains.

the peak and steady state stress. For example, peak stresses of 77 and 62 MPa and steady state stresses of 65 and 54 MPa resulted for the fast and slow strain rate experiments, respectively. Note that the onset of steady state is identical for all experiments since a constant lambda ( $\lambda$ ) of 0.4 was applied (see below).

#### 5.6. Temperatures ( $T$ )

Heat supply in real rock deformation experiments has to be calibrated using a dummy sample before running the actual deformation experiments. While during this calibration step different thermocouples are placed across the later sample position in order to achieve a homogeneous temperature profile, moving pistons variations in power supply may induce temperature shifts during the real deformation experiment. In order to account for potential variations in the deformation temperature, we evaluate in our numerical approach the effect of temperature changes of  $\pm 10 \text{ K}$  around the mean value of  $1000 \text{ K}$  (Figure 10). The total difference of  $20 \text{ K}$

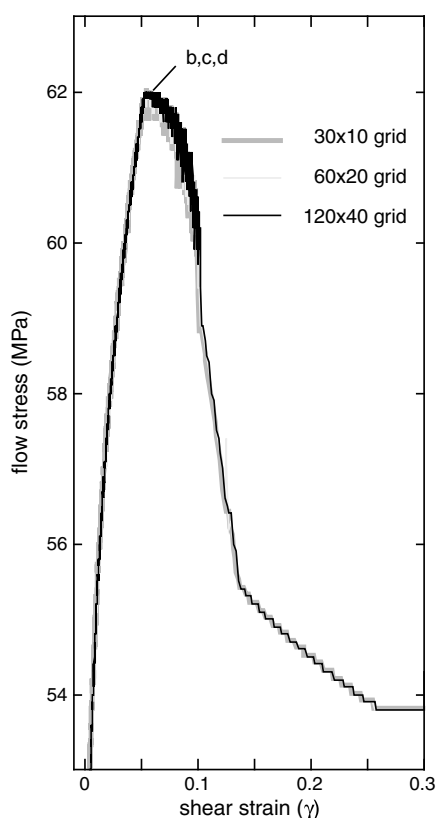


**Figure 13.** Grid sensitivity: Shear strain versus stress curves for three experiments conducted with grids of  $30 \times 10$ ,  $60 \times 20$ , and  $120 \times 40$ . The curves show excellent correlation and overlap indicating that within the used grid spacings any grid-dependent numerical artifact can be neglected. Bulk stress is obtained by averaging over the stress states of all individual grains.

weakening. While  $\lambda = 0.4$  induces a rapid stress drop to 54 MPa reached at shear strain of 0.106, values of 0.3, 0.2, 0.1, and 0.05 induce drops to 54.5, 55.5, 56.8, and 57.6 MPa at shear strains of 0.11, 0.125, 0.16, and 0.23, respectively (Figure 11). In the case of the experiment with  $\lambda = 0.01$  no steady state was reached within the experimentally applied total shear strain of 0.3. Hence, the larger the  $\lambda$ , the faster and more intense is the stress drop to steady state stresses. In terms of the microstructural expression, this variation is reflected by the steady state grain sizes, which range from 10.78 down to 7.71  $\mu\text{m}$  for  $\lambda = 0.05$  to 0.4, respectively.

When imposing the  $\lambda$  ramp, the degree of stress drop during strain weakening, the amount of grain size reduction and the resulting steady state stresses are identical compared to the constant  $\lambda$  experiments. In contrast, the timing of the onset of steady state stress and stress can be expanded by the  $\lambda$  ramp toward higher shear strains.

### 5.8. Grid Sensitivity

Generally, all the three grid sizes used display the same mechanical response with increasing shear strain (Figure 13). Slight variations in the numerical oscillations between the grids occur only near peak stresses. Here the oscillations are at maximum  $\pm 0.2$ , 0.15, and 0.1 MPa for the  $30 \times 10$ ,  $60 \times 20$ , and  $120 \times 40$  grids, respectively. Hence, all three grids show excellent reproducibility of the mechanical data allowing to run experiments at low resolution with high confidence.

Given the link between grain size and grid spacing, however, a restriction in terms of spatially highly resolved grids exists in the presented approach. The grid spacing is not allowed to be smaller than any of the average grain sizes implemented. Hence, particularly the dimension of the starting grain size defines the minimum

induces changes in peak stress from 64 to 59 MPa for peak stress and from 57 to 53 MPa for steady state stresses. Generally, the stresses are lower the higher the deformation temperature. Note that neither the absolute difference of 6–7 MPa during strain weakening nor the onset of steady state stress is affected significantly by changing the deformation temperature within the range of experimental uncertainty (Figure 10).

### 5.7. Lambda ( $\lambda$ )

The parameter  $\lambda$  documents the work required to change the microstructure. For example, the reduction in grain size needs work and the degree of  $\lambda$  is a measure of this work dissipated in the rock. In both nature and experiment, the estimation of  $\lambda$  is rather difficult. Numerical modeling represents a potential way to investigate its influence. In a first series of numerical experiments,  $\lambda$  was kept constant during the entire experiment but was varied between the experiments by choosing values of 0.01, 0.05, 0.1, 0.2, 0.3, and 0.4 (Figure 11). The same  $\lambda$  values were applied in a second set of experiments, where  $\lambda$  was ramped in a linear way from 0 to the corresponding final value during a shear increment of 0.26 (Figure 12). All these experiments were performed at a strain rate of  $1 \times 10^{-4} \text{ s}^{-1}$  and a deformation temperature of 1000 K.

In both experimental suites, the onset of strain weakening was identical in all runs in terms of stress (62 MPa) and shear strain (0.06). Variations in  $\lambda$  dramatically change the rate and the intensity of strain



allowed grid spacing. Therefore, grid spacing at steady state conditions is far away from this grain size criterion as we are dealing with fine-grained steady state grain size only.

## 6. Discussion

*Austin and Evans* [2007, 2009] and *Austin et al.* [2008] applied the paleowattmeter to evaluate the link between mechanical properties and recrystallized grain size at steady state deformation of naturally and experimentally deformed calcite. Combining UMAT in Abaqus with the paleowattmeter allows now the simulation of mechanical and grain size changes with increasing shear strain. In this way, typical stress strain curves can be generated for each element of the model consisting of (i) the initial linear elastic stress increase, (ii) nonlinear strain hardening terminated by peak stress, (iii) strain weakening, and (iv) final steady state stress (Figure 6). While (i)–(iii) represent transient stages, (iv) defines strain-invariant steady state. This mechanical evolution is the direct consequence of the interplay of elasto-visco-plastic deformation and the associated grain size changes. During the Ramberg-Osgood strain hardening until peak stress (first transient part), the average grain size increases, but the growth is best visible in small grains (Figure 6b, see lower part of diagram). Near peak stress, grain size reduction starts during the second transient part resulting in significant strain weakening for large grains (Figures 6a and 6b). Small grains with a size just slightly above the steady state one show both a limited grain size reduction and stress decrease only. In terms of deformation modes a switch from elasto-plastic to perfect plastic deformation occurs, where in the latter stage the contribution of dislocation creep and diffusion creep depends on the size of an individual grain. Note that the smaller the grains, the larger the contribution of diffusion creep. The evolution of bulk stress of the aggregate (e.g., Figures 8–10) is therefore defined by the stress-strain evolution integrated over all elements of the model.

The modeled evolution in stress and grain size qualitatively follows stress-strain curves generally found in monomineralic but polycrystalline rock deformation experiments [e.g., *Ashby and Verall*, 1977]. While the large starting grain sizes show the classical strain-hardening and weakening behavior on the way to steady state stress, small grains predominantly follow strain hardening. These two contrasting behaviors are in good agreement with the concept of steady state grain size, which was found by in situ observations from rock analogue experiments [*Herwegh and Handy*, 1996; *Herwegh et al.*, 1997], has been predicted theoretically [*de Bresser et al.*, 1998, 2001; *Shimizu*, 2008; *Austin and Evans*, 2007, 2009; *Ricard and Bercovici*, 2009], and can under ideal circumstances also be documented in nature [see *Herwegh et al.*, 2005]. Here grains too small and too large compared to the steady state grain size grow or reduce their size, respectively, to adapt it to the energetically favored steady state grains size.

Each numerical model is always just an approximation of a complex situation in reality, and it has to be calibrated. For calibration we use the calcite torsion experiments of *Pieri et al.* [2001] (compare Figures 1 and 6). As visible in Figure 1, each rock deformation experiment is affected by some degree of uncertainty despite being conducted at identical conditions. Due to this fact, the parameters in flow laws calibrated from such rock deformation experiments are also affected by uncertainty. These uncertainties were explored in a parameter study conducted with our numerical approach (see above) in order to explore the effect of variations of individual parameters. In the following we discuss what the effects of the parameters are and how they can be used for the model calibration.

### 6.1. First Strain Increments of Transient Deformation—Onset of Deformation to Peak Stress

The linear elastic part of deformation relates directly to elastic constants such as Young's modulus or the Poisson ratio and terminates in the yield stress [*Ranalli*, 1987]. Variation of these parameters within the known variability has limited effect only.

The Ramberg-Osgood strain hardening expresses the contribution of elastic and incipient plastic deformation [*Ramberg and Osgood*, 1943]. In order to accommodate these initial strains increments, different processes can be considered:

1. Intracrystalline glide along activated slip systems allow for grain internal deformation [*Etchecopar*, 1977; *Jessell*, 1988; *Lister and Hobbs*, 1980; *Wenk et al.*, 1989]. See-through rock analogue deformation experiments of *Herwegh and Handy* [1996] and *Herwegh et al.* [1997] demonstrated that this glide-induced vorticity, enclosed with rigid body rotation and intergranular glide, indeed can accommodate initial strain.

2. In the case of calcite, mechanical twinning can additionally take up shear strains up to 0.67 [Schmid *et al.*, 1987]. From a microstructural point of view, the elongation of grains and the appearance of twins are characteristic features of this incipient transient deformation [see Pieri *et al.*, 2001, Figure 8a]. It is important to note that dynamic recrystallization is limited at these deformation stages [see Herwegh and Handy, 1996, Figure 2; Pieri *et al.*, 2001, Figure 8b]. Hence, the absence of grain size reduction during the first transient stage in our numerical model is in accordance with the rock analogue and rock deformation experiments. Instead, grain growth is active, which however has limited effect on the large grains used in this numerical modeling approach but would significantly influence the mechanical behavior of small-sized aggregates as shown for the three small grains (Figure 6). Note that this grain growth effect is in agreement with recent deformation experiments performed on fine-grained calcite aggregates [Austin and Evans, 2009].

As shown in Figure 7 longer duration of Ramberg-Osgood strain hardening results in elevated peak stresses but also in a rise in steady state stress. Here adaptations in the range of about 10 MPa in stress are possible. Due to lack of micromechanical models for the minerals of interest, the termination of the Ramberg-Osgood strain hardening at the end of the first transient stage has to be arbitrarily set in the numerical model at the moment. For the application of our numerical modeling approach to naturally or experimentally deformed aggregates, a calibration of the strain increments required before the onset of dynamic recrystallization is possible. This can be derived by the microstructural study of strain series allowing the estimation of the total shear strain required before the onset of dynamic recrystallization. This value has then to be fed into the numerical model. Besides the duration of strain hardening, additional physical constraints affect the peak stress. They are treated in the next section in the context of the stress drop during strain weakening.

## 6.2. Second Part of Transient Deformation—From Peak to Steady State Stress

In our numerical models, the second part of transient deformation is defined by the degree of grain size reduction and the associated stress drop and duration of strain softening between peak stress and steady state (Figures 2 and 6). This strain weakening is of peculiar interest in Earth and materials science because it provokes strain to localize resulting in high-strain zones, i.e., so-called shear zones [Hobbs *et al.*, 1990; Montési and Zuber, 2002; Platt and Behr, 2011]. Luton and Sellars [1969], Rutter [1995], and Barnhoorn *et al.* [2005] empirically quantified the strain weakening on the base of experiments. In contrast to these studies, our approach uses the microphysical model of the Paleowattmeter, where the grain size reduction leads to an increasing contribution of diffusion creep allowing a reduction in stress. The value of peak stress in the models and the subsequent stress drop are affected by different parameters including (i) the duration of strain hardening, (ii) the preexponential factor  $K_{dis}$  of dislocation creep, (iii) the strain rate, and (iv) the deformation temperature (see Figures 7–10). Different values of  $K_{dis}$  provoke most intense variations in peak stress and strain weakening (Figure 8). Values of  $K_{dis}$  at the lower limit of experimental uncertainty reveal peak stresses twice as high as those at the upper limit. Most severe in comparison to the variations in the parameter space is the degree of stress drop in the case of  $K_{dis}$ , which decreases from  $\sim 30\%$  down to  $\sim 10\%$  for high and low  $K_{dis}$  values, respectively (Figure 8). Hence, the difficulty or ease to activate dislocation creep significantly affects peak stress and the amount of strain weakening. Microphysically, the grain size reduction in a real monomineralic mylonitic microstructure is controlled by dynamic recrystallization (subgrain rotation or bulging), where the ability of dislocations to glide and climb is crucial. Although our model does not resolve this atomic scale, the activation of dislocation creep in the grain size reduction term of the Paleowattmeter takes this effect into account.

Enhancing the strain rate from  $1$  to  $6 \times 10^{-4} \text{ s}^{-1}$  increases peak and steady state stress by  $\sim 25\%$ , while the stress drop during strain weakening just increases by  $\sim 3\%$  (Figure 9). The experimental uncertainty in temperature ( $1000 \pm 10 \text{ K}$ ) allows variations in peak and steady state stress of  $10\%$ .

In terms of the calibration of our numerical models with respect to the calcite torsion experiments of Pieri *et al.* [2001],  $K_{dis}$  is the most important parameter to be adapted followed by strain rate and temperature. The latter parameters can be used for the fine tuning. From a mechanical point of view,  $K_{dis} = 25119 \text{ MPa}^{-n_{dis}} \text{ s}^{-1}$ ,  $T = 1000 \text{ K}$ , and a strain rate of  $1 \times 10^{-4} \text{ s}^{-1}$  allowed to reproduce peak to steady state stresses, the associated stress drop during strain weakening, and the final steady state grain size observed in the rock deformation experiments most convincingly (compare Figures 1 and 6). Despite this agreement, the onset of steady state flow occurs at much lower shear strains in the numerical experiments compared to the rock deformation ones. This discrepancy must be related to the chosen values, which define how grain sizes adapt with strain on the way to steady state. In the numerical models, the grain size reduction term of the paleowattmeter (equation (16))

contains the parameter  $\lambda$ . This parameter defines the energy fraction dissipated in the microstructure. Although it is clear that at steady state most of the energy dissipated is transferred into heat [Chrysochoos and Belmahjoub, 1992], so far, there exists limited knowledge on the absolute value of  $\lambda$  and its evolution prior to steady state. The changes of  $\lambda$  in the numerical models between 0.01 and 0.4 demonstrate this effect nicely. The larger the  $\lambda$ , the more work is dissipated in the microstructure and the shorter is the grain size reduction period required to attain a steady state grain size (Figure 11). For steady state conditions, the stresses are lower the higher  $\lambda$  is (Figure 11). Hence, variations in  $\lambda$  can be used to control the shape of the strain-stress curve during strain weakening. As demonstrated by experimental investigations, grain size changes are not the only modification in a microfabric that consumes energy. Grain shapes adapt due to intracrystalline glide [e.g., Etchecopar, 1977; Means, 1981; Urai et al., 1986; Ree, 1990; Herwegh et al., 1998], domainal fabrics can evolve [Garcia Celma, 1982; Pauli et al., 1996; Herwegh et al., 1997], and even more importantly, crystallographic preferred orientations develop [Hudleston, 1980; Wilson and Russell-Head, 1982; Mancktelow, 1987; Law, 1990; Schmid and Case, 1986; Herwegh and Handy, 1996; Pieri et al., 2001; Barnhoorn et al., 2004]. All these parameters are not implicitly incorporated in our numerical model, but their bulk evolution is indirectly hidden in  $\lambda$ . In the experiments of Chrysochoos and Belmahjoub [1992]  $\lambda$  increases with increasing shear strain until it plateaus at steady state (see his Figures 11 and 12). This implies that during the initial deformation a major part of the energy is consumed in microstructures and the energy stored in the microstructure reduces to 10–20% of the total work at steady state. This behavior translates as a Taylor-Quinney coefficient of 0.9–0.8 at steady state, with much smaller values during the initial transient deformation. Such variations can be simulated with the existing model by a variety of possibilities. In the experiments presented in Figure 11,  $\lambda$  was ramped linearly over shear strains of 0.26. In this way, the duration strain weakening can be expanded. By reducing  $\lambda$  and adding a  $\lambda$  ramp, the aforementioned rapid grain size evolution and stress drop during grain softening can be slowed down and even adapted to the stress-strain curves from the real rock deformation experiments. However, this will severely increase computation time. In the future it will depend on the goal of the specific experiment. The experiment/field case dictates whether the emphasis lies on the accurate scaling in strain and stress or, alternatively, the relative difference in viscosities. The numerical models can then be designed accordingly.

## 7. Conclusions and Outlook

In this contribution we have shown a novel approach for numerically exploring the full evolution from transient to steady state deformation in an existing laboratory experiment. In this way we incorporate the empirical Ramberg-Osgood hardening model for the transient stage and the Paleowattmeter for the evolution toward steady state. This approach is important to better understand conditions leading to strain localization. Here deformational work is converted into microstructure, which later on controls the formation of shear zones at different scales. Our numerical experiments demonstrate that on the scale of the active shear zone, microstructural and mechanical homogenization is achieved. This offers a new way to model the formation and temporal evolution of shear zones using a macroscale approach where statistical grain size distribution functions describe the microstructural control of the shear zone. Furthermore, we can show that a second level of homogenization can be achieved through the emergence of characteristic localization structures within the deforming shear zone. Note that these structures are clearly formed during the transient phase.

The heart of this approach is the parameter  $\lambda$ , which defines the ratio between the energy dissipated as heat and the amount of energy stored in microstructure. Here we have presented an explorative study, where  $\lambda$  was used as a fitting parameter to integrate overall processes of energy storage in microstructure. However,  $\lambda$  could also be inferred indirectly from thermographic studies [Chrysochoos and Belmahjoub, 1992]. In such an approach an infrared camera is used to show the dissipated power  $m$  of experiments where the total work can be measured. The stored energy is simply the difference between the total and the dissipative work. We propose here that a simple modification of state-of-the-art deformation apparatus would allow the direct measurement of dissipated work in the form of heat generated. This could be achieved by replacing temperature-controlled heating units with power supply controlled ones, where heat variations in the deforming samples are measured. We suggest furthermore a parallel numerical study as performed here and a thermodynamic analysis, which would combine numerical modeling and rock deformation experiments. Such a combined analysis would shed more light on the partitioning of energies and indirectly on the physical dissipation processes operating as a consequence of the deforming microstructures.

Finally, such an approach will allow a physics-based extrapolation to large-scale localization processes as observed in the field and would add to the rigor of predicting processes at geodynamic space and time scales.

## Acknowledgments

We greatly acknowledge the constructive reviews of the Journal's referees Mark Jessell, Stefan Schmalholz, Marcin Dabrowski, Klaus Hackl, and an anonymous reviewer as well as the discussions with our colleague Manolis Veveakis, which helped to improve the article substantially. M. Herwegh acknowledges financial support from the Swiss National Science Foundation (project 200020-126560). A. Karrech, T. Poulet, and K. Regenauer-Lieb acknowledge the financial support of the Mineral Down Under Flagship of CSIRO and the Western Australian Geothermal Centre of Excellence and the University of Western Australia.

## References

- Ashby, M. F., and R. A. Verall (1977), Micromechanisms of flow and fracture, and their relevance to the rheology of the upper mantle, *Philos. Trans. R. Soc. London*, **288**, 59–95.
- Austin, N., and B. Evans (2007), Paleowattmeters: A scaling relation for dynamically recrystallized grain size, *Geology*, **35**, 343–346.
- Austin, N., and B. Evans (2009), The kinetics of microstructural evolution during deformation of calcite, *J. Geophys. Res.*, **114**, B09402, doi:10.1029/2008JB006138.
- Austin, N., B. Evans, M. Herwegh, and A. Ebert (2008), Strain localization in the Morcles Nappe (Helvetic Alps, Switzerland), *Swiss J. Geosci.*, **101**, 341–360.
- Barnhoorn, A., M. Bystricky, L. Burlini, and K. Kunze (2004), The role of recrystallisation on the deformation behaviour of calcite rocks: Large strain torsion experiments on Carrara marble, *J. Struct. Geol.*, **26**(5), 885–903.
- Barnhoorn, A., M. Bystricky, K. Kunze, L. Burlini, and J. P. Burg (2005), Strain localisation in bimineralic rocks: Experimental deformation of synthetic calcite-anhydrite aggregates, *Earth Planet. Sci. Lett.*, **240**(3–4), 748–763.
- Bons, P. D., D. Koehn, M. W. Jessell (2008), Microdynamics modelling, in *Lecture Notes in Earth Sciences*, vol. 106, 405 pp., Springer, Berlin.
- Braun, J., J. Chéry, A. N. B. Poliakov, D. Mainprice, A. Vauchez, A. Tommasi, and M. Daignières (1999), A simple parameterization of strain localization in the ductile regime due to grain size reduction, *J. Geophys. Res.*, **104**, 25,167–25,181.
- Brüggemann, R., and G. Dresen (2008), Rheology of the lower crust and upper mantle: Evidence from rock mechanics, geodesy, and field observations, *Annu. Rev. Earth Planet. Sci.*, **36**, 531–567.
- Chrysoschoos, A., and F. Belmehjoub (1992), Thermographic analysis of thermomechanical couplings, *Arch. Mech.*, **44**(1), 55–68.
- Cordier, P., J. Amodeo, and P. Carrez (2012), Modelling the rheology of MgO under Earth's mantle pressure, temperature and strain rates, *Nature*, **481**, 177–181.
- Covey-Crump, S. J. (1997), The normal grain growth behavior of nominally pure calcitic aggregates, *Contrib. Mineral. Petrol.*, **129**, 239–254.
- de Bresser, J., C. Peach, J. Reijs, and C. Spiers (1998), On dynamic recrystallization during solid state flow: Effects of stress and temperature, *Geophys. Res. Lett.*, **25**, 3457–3460.
- de Bresser, J. H. P., J. H. ter Heege, and C. J. Spiers (2001), Grain size reduction by dynamic recrystallization: Can it result in major rheological weakening?, *Int. J. Earth Sci. (Geol. Rundsch.)*, **90**, 28–45.
- Etchecopar, A. (1977), A plane kinematic model of progressive deformation in a polycrystalline aggregate, *Tectonophysics*, **39**, 121–139.
- Fan, G. J., H. Choo, P. K. Liaw, and E. J. Lavernia (2005), Plastic deformation and fracture of ultrafine-grained Alssive deformation in a polycrystalline aggregate, *Acta Mater.*, **54**(7), 1759–1766.
- Garcia Celma, A. (1982), Domainal and fabric heterogeneities in the Cap de Creus quartz mylonites, *J. Struct. Geol.*, **4**, 443–455.
- Hackl, K., and J. Renner (2013), High-temperature deformation and recrystallization: A variational analysis and its application to olivine aggregates, *J. Geophys. Res. Solid Earth*, **118**, 943–967, doi:10.1002/jgrb.50125.
- Herwegh, M., and M. R. Handy (1996), The evolution of high temperature mylonitic microfabrics: Evidence from simple shearing of a quartz analogue (norcamphor), *J. Struct. Geol.*, **18**, 689–710.
- Herwegh, M., and M. R. Handy (1998), The origin of shape preferred orientation in mylonite: Inferences from in-situ experiments on polycrystalline norcamphor, *J. Struct. Geol.*, **20**, 681–694.
- Herwegh, M., M. R. Handy, and R. Heilbronner (1997), Temperature and strain rate dependent microfabric evolution in monomineralic mylonite: Evidence from in situ deformation of a rock analogue, *Tectonophysics*, **280**, 83–106.
- Herwegh, M., X. Xiao, and B. Evans (2003), The effect of dissolved magnesium on diffusion creep in calcite, *EPSL*, **212**, 457–470.
- Herwegh, M., J. H. P. de Bresser, and J. H. ter Heege (2005), Combining natural microstructures with composite flow laws: An improved approach for the extrapolation of lab data to nature, *J. Struct. Geol.*, **27**, 503–521.
- Hobbs, B. E., B. Mühlhaus, and A. Ord (1990), Instability, softening and localization of deformation, *Geol. Soc. Spec. Publ.*, Deformation Mechanisms, *Rheol. Tectonics*, **54**, 143–165.
- Hudleston, P. J. (1980), The progressive development of inhomogeneous shear and crystallographic fabrics in glacial ice, *J. Struct. Geol.*, **2**, 189–196.
- Jessell, M. W. (1988), Simulation of fabric development in recrystallizing aggregates—II Example model runs, *J. Struct. Geol.*, **10**, 779–793.
- Jessell, M. W., P. D. Bons, L. Evans, T. Barr, and K. Stüwe (2001), Elle: The numerical simulation of metamorphic and deformation microstructures, *Comput. Geosci.*, **27**, 17–30.
- Jessell, M. W., P. D. Bons, A. Griera, L. A. Evans, and C. J. L. Wilson (2009), A tale of two viscosities, *J. Struct. Geol.*, **31**(7), 719–736.
- Karrech, A., K. Regenauer-Lieb, and T. Poulet (2011a), A damaged visco-plasticity model for pressure and temperature sensitive geomaterials, *J. Eng. Sci.*, **49**, 1141–1150.
- Karrech, A., K. Regenauer-Lieb, and T. Poulet (2011b), Continuum damage mechanics for the lithosphere, *J. Geophys. Res.*, **116**, B04205, doi:10.1029/2010JB007501.
- Karrech, A., K. Regenauer-Lieb, and T. Poulet (2011c), Frame indifferent elastoplasticity of frictional materials at finite strain, *Int. J. Solids Struct.*, **48**(3–4), 407.
- Kaus, B., and Y. Podladchikov (2006), Initiation of localized shear zones in viscoelastoplastic rock, *J. Geophys. Res.*, **111**, B04412, doi:10.1029/2005JB003652.
- Kim, Y.-J., N.-S. Huh, Y.-J. Kim, Y.-H. Choi, and J.-S. Yang (2004), On relevant Ramberg-Osgood fit to engineering nonlinear fracture mechanics analysis, *J. Pressure Vessel Technol.*, **126**(3), doi:10.1115/1.1760767.
- Knoll, M., A. Tommasi, R. E. Loge, and J. W. Signorelli (2009), A multiscale approach to model the anisotropic deformation of lithospheric plates, *Geochem. Geophys. Geosyst.*, **10**, Q08009, doi:10.1029/2009GC002423.
- Kohlstedt, D. L., B. Evans, and S. J. Mackwell (1995), Strength of the lithosphere—Constraints imposed by laboratory experiments, *Geophys. Res.*, **100**(B9), 17,587–17,602.
- Law, R. D. (1990), Crystallographic fabrics: A selective review of their application to research in structural geology, in *Deformation Mechanisms, Rheology and Tectonics*, edited by R. J. Knipe and E. H. Rutter, *Geol. Soc. Spec. Publ.*, **54**, 335–352.
- Lister, G. S., and B. E. Hobbs (1980), The simulation of fabric development and its application to quartzite: The influence of deformation history, *J. Struct. Geol.*, **2**, 355–370.

- Lister, G. S., and P. F. Williams (1983), The partitioning of deformation in flowing rock masses, *Tectonophysics*, 92, 1–33.
- Luton, M. J., and C. M. Sellars (1969), Dynamic recrystallization in nickel and nickel-alloys during high temperature deformation, *Acta Metall.*, 17, 1033–1043.
- Mancktelow, N. S. (1987), Quartz textures from the Simplon Fault Zone, Southwest Switzerland and North Italy, *Tectonophysics*, 135, 133–153.
- Means, W. D. (1981), The concept of steady-state foliation, *Tectonophysics*, 78, 179–199.
- Montési, L. G. J., and M. T. Zuber (2002), A unified description of localization for application to large-scale tectonics, *J. Geophys. Res.*, 107(B3), 2045 doi:10.1029/2001JB000465.
- Ogawa, M. (1987), Shear instability in a viscoelastic material as the cause of deep focus earthquakes, *J. Geophys. Res.*, 92, 13,801–13,810.
- Pauli, C., S. M. Schmid, and R. Panozzo Heilbronner (1996), Fabric domains in quartz mylonites: Localized three dimensional analysis of microstructure and texture, *J. Struct. Geol.*, 18, 1183–1203.
- Pieri, M., L. Burlini, K. Kunze, I. Stretton, and D. L. Olgaard (2001), Rheological and microstructural evolution of Carrara marble with high shear strain: Results from high temperature torsion experiments, *J. Struct. Geol.*, 23, 1393–1413.
- Platt, J. P., and W. M. Behr (2011), Grain size evolution in ductile shear zones: Implications for strain localization and the strength of the lithosphere, *J. Struct. Geol.*, 33, 537–550.
- Ramberg, W., and W. R. Osgood (1943), Description of stress and strain curves by three parameters, National Advisory Committee for Aeronautics (NACA) Technical Note No. 902.
- Ramsay, J. G. (1980), Shear zone geometry: A review, *J. Struct. Geol.*, 2, 83–99.
- Ranalli, G. (1987), *Rheology of the Earth*, Allen and Unwin, 366 pp., Boston, Mass.
- Ree, J. H. (1990), High temperature of octachloropropane: Dynamic grain growth and lattice reorientation, *Geol. Soc. Spec. Publ.*, Deformation Mechanisms, *Rheol. Tectonics*, 54, 363–368.
- Regenauer-Lieb, K., and D. Yuen (1998), Rapid conversion of elastic energy into shear heating during incipient necking of the lithosphere, *Geophys. Res. Lett.*, 25, 2737–2740.
- Regenauer-Lieb, K., and D. A. Yuen (2003), Modeling shear zones in geological and planetary sciences: Solid- and fluid-thermal-mechanical approaches, *Earth Sci. Rev.*, 63, 295–349.
- Regenauer-Lieb, K., and D. A. Yuen (2004), Positive feedback of interacting ductile faults from coupling of equation of state, rheology and thermal-mechanics, *Phys. Earth Planet. Inter.*, 142(1–2), 113–135.
- Regenauer-Lieb, K., and D. A. Yuen (2008), Multiscale brittle-ductile coupling and genesis of slow earthquakes, *Pure Appl. Geophys.*, 165, 523–543.
- Renner, J., and B. Evans (2002), Do calcite rocks obey the power-law creep equation?, in *Deformation Mechanisms, Rheology and Tectonics: Current Status and Future Perspectives*, *Geol. Soc. London*, edited by S. de Meer et al., 200, 293–307.
- Ricard, Y., and D. Bercovici (2009), A continuum theory of grain size evolution and damage, *J. Geophys. Res.*, 114, B01204, doi:10.1029/2007JB005491.
- Rosakis, P., A. J. Rosakis, G. Ravichandran, and J. Hoodwink (2000), A thermodynamic internal variable model for the partition of plastic work into heat and stored energy in metals, *J. Mech. Phys. Solids*, 48, 581–607.
- Rozel, A., Y. Ricard, and D. Bercovici (2011), A thermodynamically self-consistent damage equation for grain size evolution during dynamic recrystallization, *Geophys. J. Int.*, 184, 719–728.
- Rutter, E. H. (1974), The influence of temperature, strain rate and interstitial water in the experimental deformation of calcite, *Tectonophysics*, 22, 311–384.
- Rutter, E. H. (1995), Experimental study of the influence of stress, temperature, and strain on the dynamic recrystallization of Carrara marble, *J. Geophys. Res.*, 100, 24,651–24,663.
- Rutter, E. H. (1999), on the relationship between the formation of shear zones and the form of the flow law for rocks undergoing dynamic recrystallization, *Tectonophysics*, 303, 147–158.
- Schmalholz, S., B. J. Kaus, and J. P. Burg (2009), Stress-strength relationship in the lithosphere during continental collision, *Geology*, 37, 775–778.
- Schmid, S. M., and M. Case (1986), Complete fabric analysis of some commonly observed quartz c-axis patterns, in *Mineral and Rock Deformation: Laboratory Studies—The Patterson Volume*, 36, 161–199, AGU, Washington, D. C.
- Schmid, S. M., and M. R. Handy (1991), Towards a genetic classification of fault rocks: Geological usage and tectonophysical implications, in *Controversies in Modern Geology*, edited by D. W. Müller, J. A. McKenzie, and H. Weissert, pp. 95–110, Academic Press, London, U.K.
- Schmid, S. M., M. S. Paterson, and J. N. Boland (1980), High temperature flow and dynamic recrystallization in Carrara marble, *Tectonophysics*, 65, 245–280.
- Schmid, S. M., R. Panozzo, and S. Bauer (1987), Simple shear experiments on calcite rocks: Rheology and microfabric, *J. Struct. Geol.*, 9(5/6), 747–778.
- Shimizu, I. (2008), Theories and applicability of grain size piezometers: The role of dynamic recrystallization mechanisms, *J. Struct. Geol.*, 30, 899–917.
- Skelton, R. P., H. J. Maier, and H.-J. Christ (1997), The Bauschinger effect, Masing model and the Ramberg shear experiments on calcite rocks: Rheology a, *Mater. Sci. Eng. A*, 238(2), 377–390.
- Urai, J. L., W. D. Means, and G. S. Lister (1986), Dynamic recrystallization of minerals, *AGU Geophys. Monogr.*, 16, 161–199.
- Wenk, H.-R., G. Canova, A. Molinari, and U. F. Kocks (1989), Viscoplastic modelling of texture development in quartzite, *J. Geophys. Res.*, 94, 17,895–17,906.
- Wilson, C. J. L., and D. S. Russell-Head (1982), Steady-state preferred orientation of ice deformed in plane strain at –1°C, *J. Glaciol.*, 28, 145–160.